

Exomorphism of jacobsite precipitates in bixbyite single crystals from the Thomas Range in Utah

JOHANNES PETER^{1,*}, MAXIMILIAN TRAPP¹, STEFAN LAUTERBACH¹, PHILIPP GOLLÉ-LEIDREITER¹,
UTE KOLB^{1,2}, AND HANS-JOACHIM KLEEBE¹

¹Institute of Applied Geosciences, Technical University of Darmstadt, Schnittspahnstrasse 9, D-64287 Darmstadt, Germany

²Institute of Physical Chemistry, Johannes Gutenberg University, Duesbergweg 10-14, D-55128 Mainz, Germany

ABSTRACT

Naturally occurring single crystals of bixbyite, $(\text{Fe,Mn})_2\text{O}_3$, from the Thomas Mountain Range in Utah, U.S.A., were studied via (scanning) transmission electron microscopy (S)TEM. With up to 5 cm edge length, these mineral specimens are the largest bixbyite crystals found worldwide. Their hexahedral shapes are often modified by $\{211\}$ facets at the corners and small $\{211\}$ truncations along their cube edges. Characteristic lamellar defects, running parallel to the $\{100\}$ planes, can be observed via TEM imaging. The defects are, according to EDS analyses, attributed to the tetragonal manganese silicate braunite, $\text{Mn}_7[\text{SiO}_{12}]$. In the present study, electron nano-diffraction and atomic resolution (S)TEM were employed to verify the presence of braunite lamellae and to investigate their orientation relationship with bixbyite. The analysis confirmed an epitaxial intergrowth of both phases, with their main-axes being parallel and the unique c -axis of braunite always aligned perpendicularly to the lamellar plane. Moreover, small rectangular-shaped precipitates, which had been, due to their almost identical chemical composition, previously interpreted as small bixbyite inclusions within the host crystal, were often observed in contact with the braunite lamellae. Electron nano-diffraction and atomic resolution (S)TEM imaging revealed these crystallites not to be bixbyite but jacobsite, a cubic iron-manganese spinel with the stoichiometric formula MnFe_2O_4 , whose occurrence in this unique context had not been reported before. Moreover, due to the higher temperatures needed for spinel crystallization, the occurrence of jacobsite may serve as a geo-thermometer. (S)TEM in conjunction with automated crystal orientation mapping (ACOM)-TEM showed that no orientation relationship exists between the jacobsite inclusions and the bixbyite/braunite matrix. Nevertheless, their characteristic rectangular shape is typically aligned concordantly with the (001) plane of the braunite lamellae. The resulting crystal shape of jacobsite is determined by the presence of the braunite lamellae, while the respective crystallites maintain their freedom of rotation. To the authors' knowledge, this is a novel observation of exomorphosis of jacobsite, i.e., the change in the habit of the spinel crystallites due to external conditions. Note that the term “exomorphosis” is used here in the mineralogical sense in contrast to the often-used petrological aspect. Based on the TEM results, the formation of the jacobsite precipitates is discussed and a growth model suggested.

Keywords: TEM, ACOM, spinel, bixbyite, braunite, diffraction

INTRODUCTION

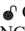
In geoscience, the term “exomorphosis” is commonly used in petrology and denotes contact metamorphism due to a magmatic intrusion or lava flow. However, in this paper, the term is used according to its mineralogical definition, which describes the dependence of crystal habit or shape and occurring crystal facets on the local chemophysical environment (Kleber 1957).

As first described by Penfield and Foote, bixbyite is a rarely occurring natural iron-manganese-oxide mineral typically showing isometric hexahedral habit, exhibiting an octahedral cleavage and a hardness of 6–6.5 (Penfield and Foote 1897). While the authors initially suggested an orthorhombic or cubic perovskite structure with the formula FeMnO_3 , later Laue diffraction investigations performed in 1928 revealed the unit cell to be body-centered

cubic with a cell parameter of $a = 9.365 \text{ \AA}$ (Zachariasen 1928). Consequently, Zachariasen proposed the formula $(\text{Fe,Mn})_2\text{O}_3$, being a solid solution of Fe_2O_3 and Mn_2O_3 , while he also realized a close relationship between bixbyite and certain sesquioxides of type M_2O_3 (with $\text{M} = \text{Al, Fe, or RE elements}$, for example), as also reported by V.M. Goldschmidt, based on recorded diffraction patterns (Goldschmidt 1926).

An investigation of the tetragonal pseudo-cubic mineral braunite, $\text{Mn}_7[\text{SiO}_{12}]$, by L. Pauling and M.D. Shappell in 1930, found its unit-cell structure to be closely related to that of bixbyite, having dimensions almost identical to those of two superimposed bixbyite unit cells (Pauling and Shappell 1930). This triggered a reexamination of the bixbyite structure proposed earlier by Zachariasen, who had postulated the space group $I2_13$ (no. 199). While he had correctly determined the body-centering of the unit cell via the absence of $\{0kl\}$ reflections, with the incident beam normal to $\{100\}$ plane, it was concluded that only the space group $Ia\bar{3}$ (no. 206) holds for the observed pattern and, therefore, corresponds to

* E-mail: peter@geo.tu-darmstadt.de

 Open access: Article available to all readers online. This article is CC-BY-NC-ND.

the bixbyite structure. In the following years, more detailed structural investigations were performed; however, all confirmed the $Ia3$ space group, representing the C-modification of M_2O_3 -type sesquioxides (Patterson 1939; Fleischer 1943; Menzer 1949; Dachs 1956; Strunz and Nickel 2001).

In 1944, B. Mason investigated the Fe_2O_3 - Mn_2O_3 phase diagram, addressing the ongoing discussion about the appropriate mineral names of the bixbyite solid-solution series (Mason 1944). He suggested a division of the $(Mn,Fe)_2O_3$ group of minerals into two subgroups based on their formation conditions. According to his results, bixbyites are minerals containing 45–60 mol% Fe_2O_3 , forming at rather high-temperatures (800–1000 °C), which corresponds to a pneumatolytic origin, while he proposed that specimens with <30 mol% Fe_2O_3 should be named sitaparite, representing a lower temperature (<650 °C) metamorphic formation. According to his phase diagram, the bixbyites from the Thomas Mountain Range contain around 50 at% Fe_2O_3 and should therefore be considered of pneumatolytic origin, reflecting their formation from a cooling rhyolitic magma.

The mineral braunite was first described by W. Haidinger, while its crystal structure remained unresolved until the early 1940s (Haidinger 1828). In 1931, the space group $I4_1/acd$ was proposed by G. Arminoff, while in 1943, A. Byström and B. Mason postulated $I4c2$, based on their crystal-structure analysis data. Only the latter study revealed the correct formula for braunite: $3 \cdot Mn_2O_3 \cdot MnSiO_3$ (Arminoff 1931; Byström and Mason 1943). It was not until 1967, that J.P.R. de Villiers and F.H. Herbstein solved the crystal structure with space group, $I4_1/acd$, from single-crystal investigations of braunites from various localities, confirming the space group proposed by G. Arminoff (de Villiers and Herbstein 1967).

A thorough investigation of the close structural relationship between bixbyite and braunite was first published in 1976, followed by other authors in the upcoming years (Moore and Araki 1976; Abs-Wurbach 1980; de Villiers and Buseck 1989). It was concluded that the structures of both minerals can be described as sheets of edge- and corner-linked octahedra, with cubic bixbyite consisting only of A-sheets, whereas in braunite every second A-sheet is replaced by a B-sheet, containing Mn^{2+} in cubic, Mn^{3+} in octahedral and Si^{4+} in tetrahedral coordination as depicted in Figure 1. The cation positions of braunite closely correspond to those of Mn_2O_3 , with one-half of the octahedral Mn^{3+} replaced by Si^{4+} in the B-sheet, while charge balance is maintained by divalent Mn^{2+} cations in hexahedral coordination. Moreover, in their studies of different layer stackings in the system bixbyite-

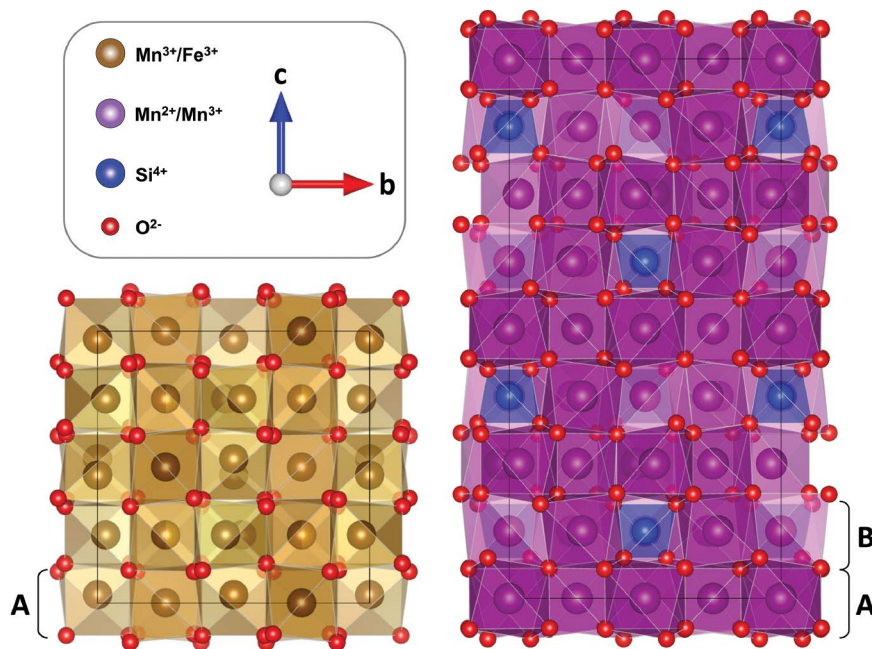


FIGURE 1. Schematics showing the crystal structure of bixbyite (left) and braunite (right) created with VESTA software (Momma and Izumi 2008). While the cubic bixbyite consists only of A-sheets, in the braunite structure, every second A-sheet is replaced by a B-sheet, which contains Mn^{2+} in cubic, Mn^{3+} in octahedral and Si^{4+} in tetrahedral coordination. The orientation of both crystal structures is indicated in the upper left corner.

braunite, J.P.R. de Villiers and P. Buseck showed that some bixbyites, which were supposed to be single crystals, in fact exhibit non-stoichiometry and anisotropy due to their stacked-layer intergrowth with braunite (de Villiers and Buseck 1989). Also, bixbyite coherently intergrown with layers of braunite-II, a calcium-bearing variety of braunite, was studied by J.P.R. de Villiers via HRTEM imaging (de Villiers 1980). The images showed no distortion at the layer interfaces, thereby forming a strainless polysomatic structure of both phases.

Bixbyites may be found in seams and cavities of the rhyolitic host rock at various localities in the Thomas Mountain Range, Utah, U.S.A. Specimens from the Solar Wind Claim are known to occur in crystals of up to 5 cm edge length, being the largest worldwide and, interestingly, are considerably larger than bixbyites found at other mineral discoveries in the Thomas Mountain Range. The larger crystals often show characteristic $\{211\}$ surface facets at the corners as well as $\{211\}$ truncations at their cube edges (Fig. 2). Furthermore, these truncations are linked by bands of linear features crossing the cube faces parallel to $\{100\}$, which is a peculiarity not observed on small crystals with unmodified hexahedral morphology.

In 2008, H.-J. Kleebe and S. Lauterbach studied large bixbyite single crystals from the Solar Wind Claim via electron microscopy, investigating the internal structure and exaggerated crystal growth (Kleebe and Lauterbach 2008). Their results indicated that the linear surface features, formerly interpreted as twin-boundaries, are congruently intergrown braunite lamellae, forming a complex 3D-network throughout the host crystal, possibly triggering the formation of the $\{211\}$ surface facets along the cube corners

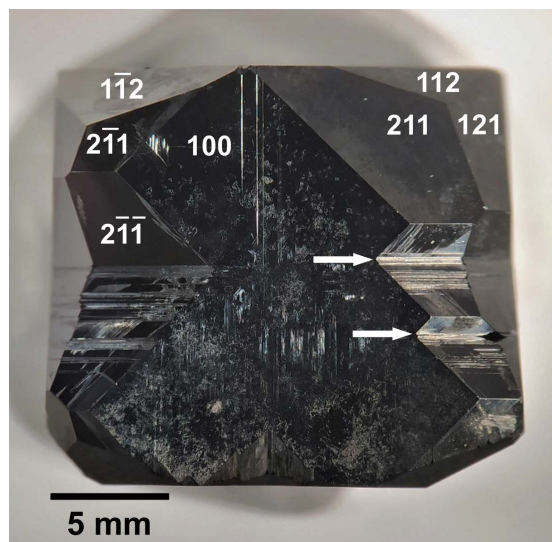


FIGURE 2. Photograph of a large bixbyite crystal from the Solar Wind Claim, exhibiting hexahedral morphology modified by $\{211\}$ surface facets at the cube corners as well as $\{211\}$ truncations on the edges (arrows).

when reaching the crystal surface. In addition, their investigations revealed the presence of small inclusions, which were differentiated into two types. While the type-I inclusions are rather irregularly shaped secondary phases randomly occurring within the bixbyite bulk, type-II inclusions not only exhibit well-defined rectangular shapes oriented parallel to braunite lamellae, they were also always observed in direct contact to those. Based on EDS measurements, type-I inclusions were attributed to topaz, quartz, and rutile, whereas type-II inclusions were interpreted as small bixbyite precipitates. Although within the proposed growth model, suggestions were given regarding the formation of these type-II inclusions, the main focus was on the braunite lamellae. Therefore, some open questions remained, especially on the existence of a possible orientation relationship between type-II inclusions and braunite or bixbyite. Since the braunite lamellae and bixbyite host crystal showed a distinct epitaxial intergrowth, it can be assumed that, at least, preferred orientations exist also for the bixbyite precipitates. To clarify these questions as well as to verify previous results, the present electron microscopy study was conducted on the crystal structure and chemistry of bixbyites from the Solar Wind Claim in the Thomas Mountain Range.

EXPERIMENTAL PROCEDURES

Three individual TEM-samples were prepared. Two were made from a large cubic single crystal with ~ 3 cm edge length and a third one from a smaller single crystal of around 1 cm in size. For each sample, a slice of ~ 500 μm thickness was cut parallel to a $\{100\}$ crystal face. Subsequently, 3 mm disks were cut from those regions of the slices that showed the highest quantity of lamellae and linear features during inspection with an optical microscope. The resulting disks were polished on both sides down to a thickness of 20 μm using an Allied MultiPrep Polishing System (Allied High Tech Products, Inc., Rancho Dominguez, California, U.S.A.) with different diamond lapping films (9, 6, 3, and 1 μm) and mounted on a supporting molybdenum TEM-grid (100 mesh), using a two-component epoxy resin.

To reach electron transparency, the samples were thinned by a two-step argon-ion milling procedure using a Gatan DuoMill 600 (Gatan, Inc., Pleasanton, California, U.S.A.). In the first step, an acceleration voltage of 4.5 kV and an incidence angle of 14° was maintained until small holes were visible in the light microscope. Further ion-milling, with an acceleration voltage of 2 kV and an incidence angle of 12° , was

applied for 15 min to remove amorphous residue and clean the sample surface. Finally, all samples were lightly coated with carbon (~ 5 nm thick) to minimize charging under the incident electron beam.

Conventional transmission electron microscopy (TEM), including electron diffraction and high-resolution imaging, was performed with a JEOL (JEOL, Akishima-shi, Tokyo, Japan) JEM-2100F, while high-angle annular dark-field (HAADF) and annular bright-field (ABF) images were obtained using a JEOL JEM ARM-200F, equipped with a C_s -corrector (CEOS GmbH, Heidelberg, Germany). In both microscopes, a JEOL beryllium double tilt holder enabled sample orientation along specific zone axes. EDS spectra were acquired with an Oxford XMAX 80 detector (Oxford Instruments plc, Tubney Woods, Abingdon, U.K.).

Automated crystal orientation mapping (ACOM) TEM data was collected using the JEOL JEM-2100F, equipped with an ASTAR system and a Digistar precession unit, developed by NanoMegas company (NanoMEGAS SPRL, Brussels, Belgium). An ultrafast external CCD camera Stingray F-145B (Allied Vision, Stadroda, Germany), with up to 200 fps, was used to record precession electron diffraction (PED) patterns from the phosphor screen. The Data Acquisition was done in TEM mode with spot size 5, α_2 convergence angle, and the smallest condenser aperture (10 μm). These settings resulted in a probe size of around 10 nm. The precession unit was operated at 100 Hz, allowing an acquisition rate of up to 100 PED patterns per second, with a precession angle of 0.65° , using a camera length of 12.3 cm. Image distortions and the camera length error introduced by the inclination of the screen relative to the recording camera were corrected during data processing with the ASTAR software. A database of diffraction patterns from bixbyite and jacobsite was simulated from previously reported structure files (Pauling and Shappell 1930; Lucchesi et al. 1996), available in the Crystallography Open Data Base (Grazulis et al. 2009).

The experimental PED patterns are compared to all simulated diffraction patterns and matched through the calculation of a correlation index value (Q) (Rauch and Véron 2014). The solution assigned to each experimental pattern corresponds to the highest correlation index value, i.e., the template with the highest degree of matching. Naturally, diffraction patterns with more than one possible phase or orientation solution (for instance, at grain boundaries), yield more than one high correlation index value. Consequently, a reliability index value (R) is derived from the ratio of the two optimum solutions Q_1 and Q_2 with $R = 100(1 - Q_2/Q_1)$ (Rauch and Véron 2014). Reliability and correlation index maps display their respective value in grayscales ranging from minimum (black) to maximum (white). Therefore, reliability maps may show phase or grain boundaries as distinctive dark features.

EXPERIMENTAL RESULTS

The TEM investigation revealed the presence of thin braunite lamellae in all three samples, always running parallel to the $\{100\}$ planes of the bixbyite host crystal and occasionally forming stair-stepping patterns or perpendicular line-systems. As previously described, these findings are indicative of a 3D-network of the braunite lamellae (Kleebe and Lauterbach 2008). In between the bixbyite reflections, selected-area electron diffraction (SAED) of lamellae-rich regions revealed additional faint reflections elongated in the c^* -direction (Fig. 3a). By generating a dark-field (DF) image using these reflections, all parallel lamellae of one group appear homogeneously bright on a dark background (Fig. 3b), indicating that they all have the same orientation relative to the host crystal.

Moreover, as is expected for a perfect epitaxial intergrowth of bixbyite and braunite, TEM imaging revealed no indications of strain at the interfaces between the host crystal and braunite lamellae. Electron nano-diffraction conducted on individual braunite lamellae revealed reflections with half the reciprocal distance for $(00l)$ reflections, corresponding to a doubled lattice plane spacing orthogonal to the lamellar planes (Fig. 4).

Since the braunite unit cell is double that of bixbyite along the $[001]$ unit-cell direction, the c -axis direction of braunite can be determined from the diffraction patterns by the observation of reflection rows with half the reciprocal distances compared to the $\{001\}$ bixbyite type. In all cases, the c -axis of braunite was found to be oriented perfectly perpendicular to the corresponding lamellar

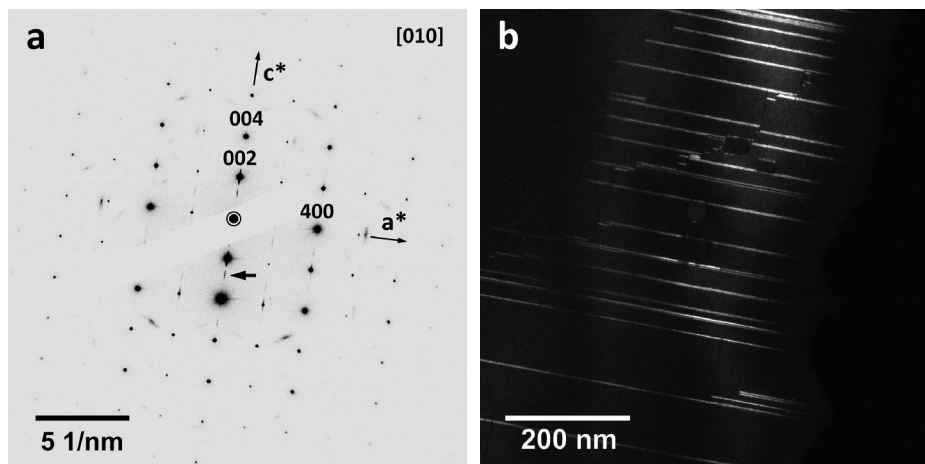


FIGURE 3. SAED pattern (a) of bixbyite along [010] with faint elongated reflections between those relating to the host crystal's lattice. The DF image (b), generated by using the reflection marked by the arrow in the diffraction pattern, shows parallel running lamellae bright on dark background, indicating a uniform orientation.

plane (see Fig. 4). Furthermore, since the superimposed patterns of bixbyite and braunite show the same reflection intervals in directions perpendicular to [001] of braunite, i.e., the [100] for example, the observations imply that all main directions of both phases run parallel to each other (compare also Fig. 1).

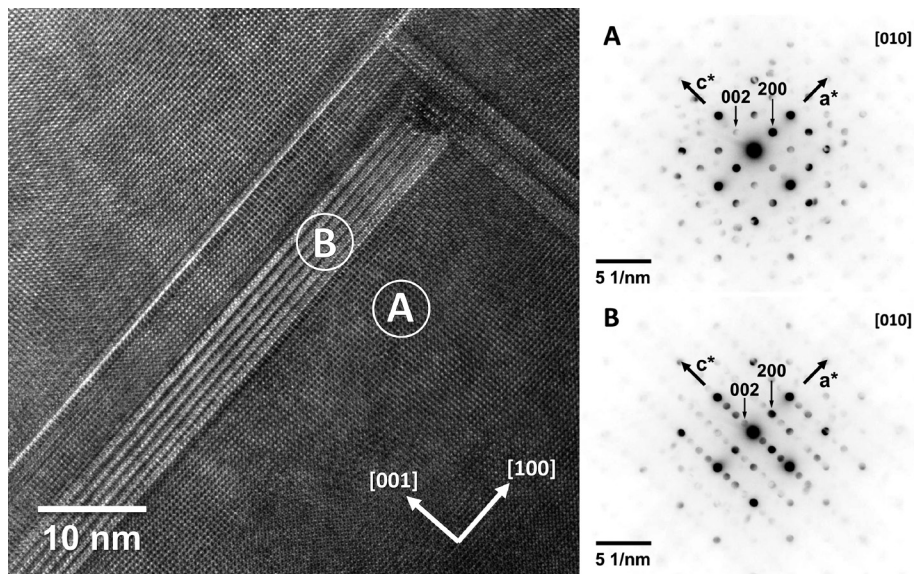
It is concluded that the very small deviation of the (100) lattice plane spacings of both phases (9.365 Å for bixbyite and 9.432 Å for braunite, respectively) allows for the observed perfect epitaxial intergrowth along these planes. Furthermore, in the [001] direction an equally good fit exists between the (001) bixbyite (9.365 Å) and the (002) braunite (9.352 Å) lattice planes. Therefore, the perfect epitaxial intergrowth can easily expand to a 3D-network. It is worth mentioning that most examined lamellae have a thickness of around 19 Å, corresponding to a single *c*-axis length of the unit cell. However, double and triple width lamellae were also observed, which equal an integer multiple of the single unit-cell parameter. Please note that the presence of multiple lamellae with

varying thicknesses and distances to each other typically causes a streaking and elongation of corresponding diffraction spots, as shown for braunite in Figure 3a.

Throughout the entire host crystal and always in contact with the braunite lamellae, rectangularly shaped precipitates, between 20 and 50 nm in size, were observed in the samples prepared from the large crystal (Figs. 5a and 5b). Interestingly, no such inclusions were evident in areas devoid of braunite lamellae, and none were found in the third sample (smaller crystal) in the examined areas. Furthermore, since the crystal edges are aligned concordantly with the lamellae, a genetic relationship of both phases is indicated.

According to EDS analyses, these precipitated crystallites have the same chemical composition as the host crystal, with iron, manganese, and oxygen being their main constituents (Fig. 5d). To identify the present phase, several inclusions were oriented parallel to a low-indexed zone axis and examined via electron nano-diffraction. The tilting angle relative to the [010] zone axis of the bixbyite host

FIGURE 4. HRTEM image of a braunite lamella and the surrounding bixbyite lattice (left). Both phases are oriented simultaneously and no strain is visible along their interface; (right) comparison of electron nano-diffraction patterns of the host crystal (A) and the braunite lamella (B). The reciprocal lattice spacing of braunite in [001]-direction is halved, revealing the orientation of its *c*-axis being perpendicular to the lamella plane.



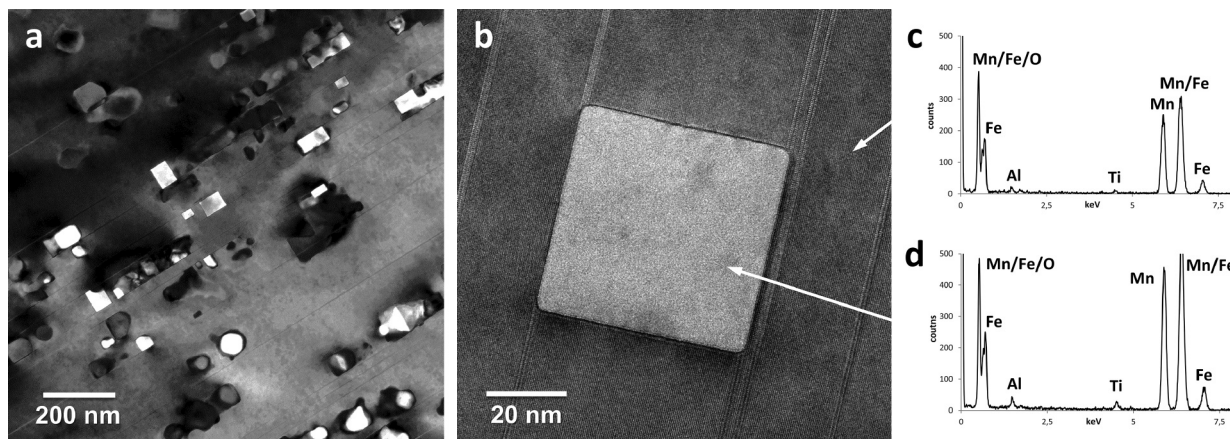


FIGURE 5. TEM bright-field overview (a), showing numerous rectangular shaped precipitates in direct contact with braunite lamellae. Crystallites not attached to but near lamellae exhibit an irregularly rounded morphology. The HRTEM image in b displays an almost square-shaped crystallite bordered by lamellae on two sides. EDS measurements show that the chemical composition of the bixbyite host crystal (c) and the precipitate (d) is almost identical regarding the main components manganese, iron, and oxygen. Alumina and titanium are incorporated in trace amounts in both phases.

crystal, which was used as reference orientation, was recorded to determine whether an epitaxial relationship between both phases was present. The entire set of patterns obtained could be indexed self-consistently only as jacobsite $(\text{Mn}^{2+}, \text{Fe}^{2+})(\text{Mn}^{3+}, \text{Fe}^{3+})_2\text{O}_4$, a rare cubic iron-manganese spinel ($Fd\bar{3}m$, $a = 8.505 \text{ \AA}$) (Essene and Peacor 1983; Beard and Tracy 2002; Gottesmann et al. 2015), not previously known to occur in this location. This is in contrast to an earlier study, where the precipitation of nanosized bixbyites within the large host crystal was proposed (Kleebe and Lauterbach 2008). However, this contradiction can be explained by the high similarity of the respective diffraction patterns in many orientations, especially in the case of low-indexed zone axes. Nevertheless, a bixbyite crystal structure can be ruled out since it is not possible to unambiguously index all of the recorded diffraction patterns as bixbyite in our new data set.

Interestingly, the recorded tilt angles between host crystal and precipitate were significantly different for every individual crystallite, even when identical zone axes were oriented. In fact, these observations strongly indicated that each jacobsite crystallite has a different unique orientation of its own. Furthermore, it can be concluded that no simple orientation relationship exists neither between the jacobsite nano-crystals and the bixbyite host crystal nor between the spinels and the braunite lamellae, although this was initially assumed due to the crystallites' coherently aligned rectangular shape (Fig. 5).

Subsequent to the diffraction measurements, high-resolution STEM studies of the inclusions, aiming to unequivocally identify the nano-sized crystallites, were carried out. High-angle annular dark-field (HAADF) and annular bright-field (ABF) images of oriented crystallites were obtained and compared to simulations of the jacobsite lattice in its respective orientation. An atomic-resolution HAADF image of a jacobsite crystallite is displayed in Figure 6. The spinel is oriented along its $[\bar{1}10]$ zone axis, with the surrounding bixbyite lattice revealing no specific orientation. The inset in Figure 6b shows a lattice simulation, generated via QSTEM (Koch 2002), for a specimen thickness of 30 nm and an acceptance angle (i.e., the angle of the signal collection on the detector plate)

of 90–370 mrad. It is evident that the simulated cation positions almost exactly coincide with the cation column positions of the electron micrograph. The complementary ABF image given in Figure 7 shows a similarly high agreement with its corresponding simulation in the inset of Figure 7b for the same thickness and an acceptance angle of 11–22 mrad. Note that in this particular imaging mode, the oxygen column positions are revealed, marked with arrows in both image and simulation.

To investigate the jacobsite precipitates regarding their complex orientation relationship and preferential orientation in general, ACOM-TEM measurements were conducted. An area of $\sim 1 \mu\text{m}^2$ containing several spinel crystallites, as depicted in the bright-field (BF) image of Figure 8a, was scanned in steps of 1 nm. Since the orientation of bixbyite and braunite is known and the distinction between these phases was not the focus of this investigation, braunite templates were not used for indexing. In Figure 8b, a combination of the phase map with the phase reliability map is shown. Dark features in the map show low reliability values, accentuating grain boundaries, where the diffraction patterns of jacobsite and bixbyite/braunite overlap. As evident from this combined image, most rectangular-shaped crystallites were confidently identified by the software as jacobsite, showing high reliability values. However, not all contrast features that appeared to be jacobsite crystallites were indexed as such (some of them are marked by arrows in the BF image). Their corresponding diffraction patterns equal that of the surrounding bixbyite lattice. It is concluded that the observed contrast can only be attributed to thickness variations, most likely due to jacobsite crystallites that were partially removed during the ion thinning procedure resulting in a pronounced surface topography. Several precipitates that appear not to be in contact with braunite lamellae and display irregular crystal faces were also recognized as spinel. This counteracts the assumption that the crystallization of jacobsite is directly related to the formation process of the braunite lamellae. However, it indicates that the contact to the lamellae leads to the observed rectangular shape of the respective precipitates.

Figures 8c to 8e depict the z , x , and y crystallographic orientation of the mapped jacobsite precipitates, respectively. The uniform

FIGURE 6. Fourier-filtered HAADF image, (a) of a precipitate along its $[110]$ zone axis surrounded by the non-oriented bixbyite lattice obtained with a camera length of 6 cm. (b) shows a higher magnification of the crystallite's lattice in the boxed area. The inset depicts a QSTEM (Koch 2002) lattice simulation for an acceptance angle of 90–370 mrad and a sample thickness of 30 nm.

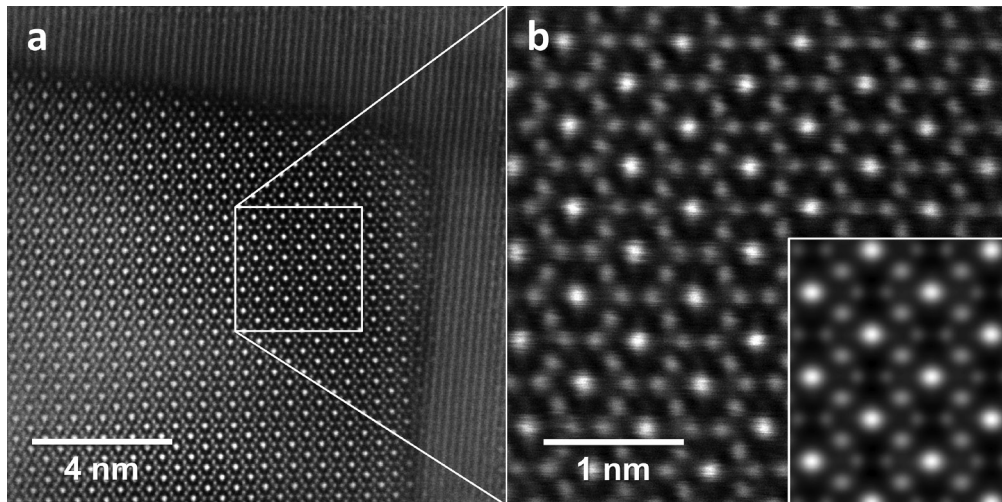
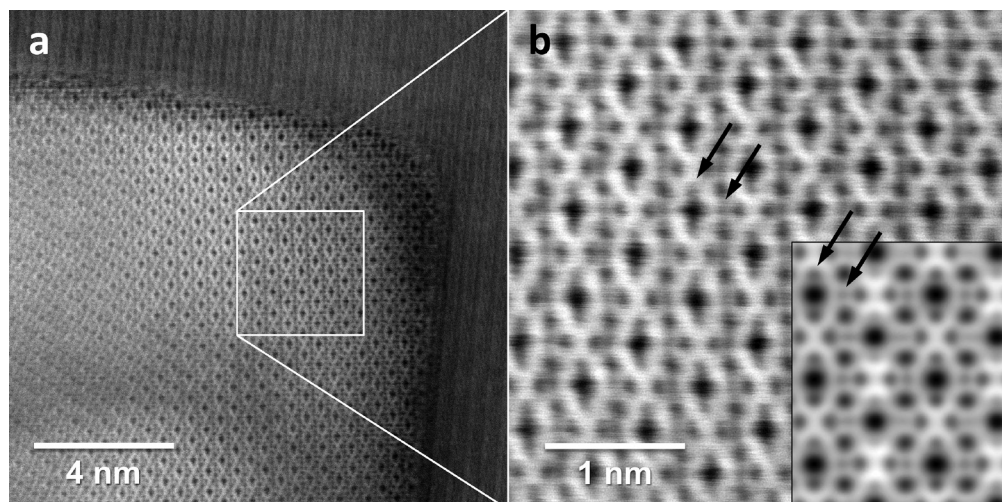


FIGURE 7. Fourier-filtered ABF image, (a) of a precipitate along its $[110]$ zone-axis surrounded by the non-oriented bixbyite lattice obtained with a camera length of 6 cm. In b, a higher magnification view of the imaged lattice in the boxed area is given. The inset shows a QSTEM (Koch 2002) lattice simulation for an acceptance angle of 11–22 mrad and a sample thickness of 30 nm. The oxygen positions are marked with arrows in both image and simulation.



$[010]$ -orientation of the bixbyite/braunite lattice is not displayed here, i.e., the black background represents the host crystal, whereas the various orientations of the jacobsite crystallites are depicted according to the color legend. While Figure 8c shows several precipitates in or close to their $[111]$ zone axis, it is evident from Figures 8d and 8e that numerous individuals are rotated around this axis and, therefore, are differently oriented with respect to the host crystal lattice. Moreover, no indication of a preferential orientation was found regardless of the jacobsites exhibiting rectangular shapes along the braunite lamellae or being irregularly shaped. Despite their similar cell parameters and their almost identical composition, an epitaxial or any other orientational relationship between the bixbyite host crystal and the jacobsite precipitates could be excluded.

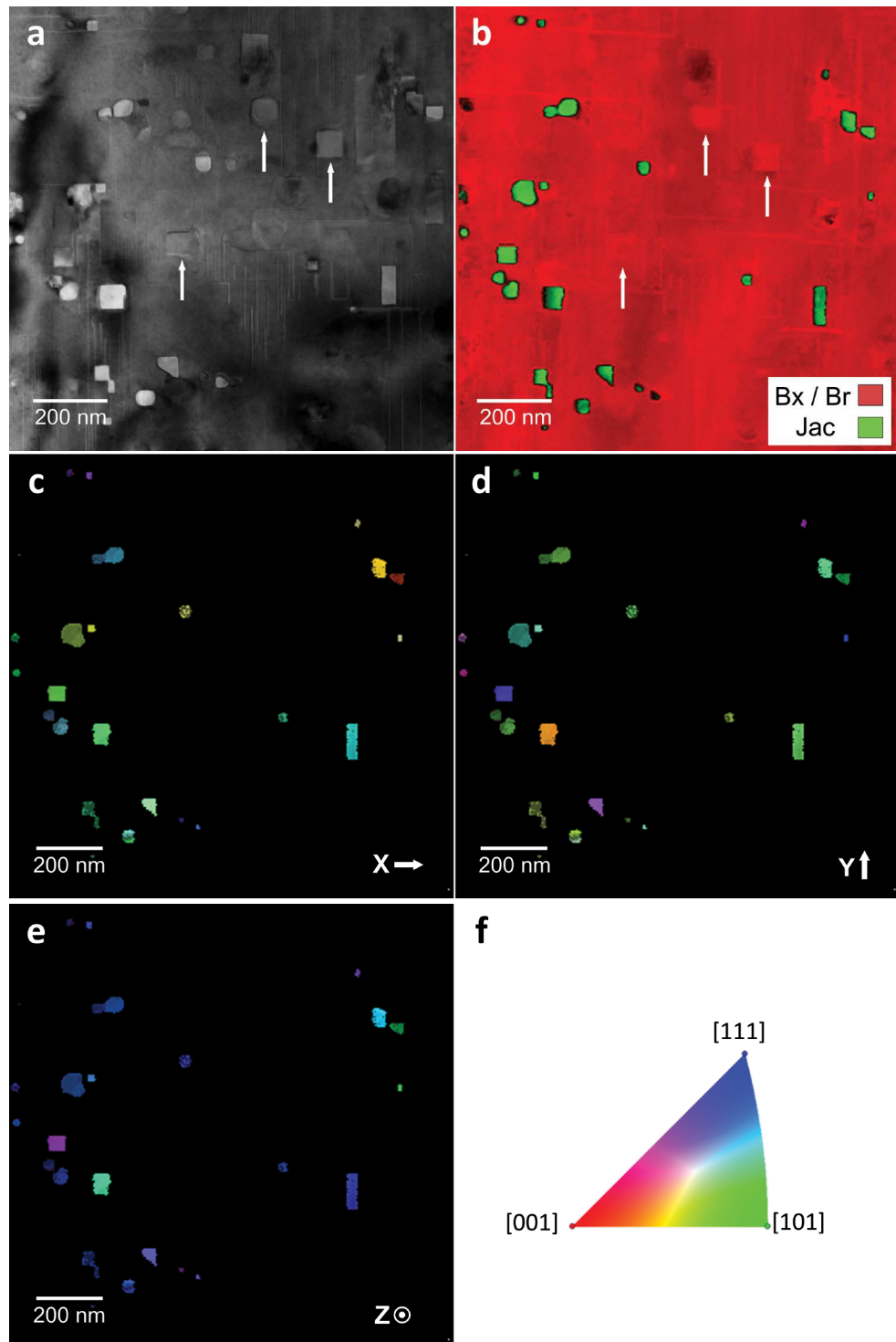
DISCUSSION

Using the layer model presented by de Villiers, the formation of the braunite lamellae can be understood as follows. Bixbyite and braunite share an almost identical A-layer and differ from each other only by the existence of a Si^{4+} -containing B-layer in Braunite (de Villiers 1980). As discussed in more detail in a previous publica-

tion (Kleebe and Lauterbach 2008), it is proposed that a slightly elevated silicon content of the mother solution in the hydrothermal crystallization process can be compensated via the deposition of silicon bearing B-layers on the preexisting A-layers of the host crystal, which is obviously energetically more favorable as compared to the formation of, for example, other SiO_2 -bearing phases such as quartz or topaz, both known from the Thomas Mountain Range. After a sufficiently high incorporation of silicon, the formation of braunite lamellae stops, and the host crystal continues to grow more silicon-free A-layers, i.e., the regular bixbyite growth continues. The perfectly coherent interface between the braunite lamellae, running parallel to the $\{100\}$ planes of the host crystal, and the bixbyite is shown in Figure 9. This perfect intergrowth of the $\text{Mn}_7\text{SiO}_{12}$ lamellae and bixbyite is a consequence of the almost identical cell parameters of the two participating lattices, giving a strain-free phase boundary in a -, b -, and c -direction of the unit cell.

However, to understand the formation of the jacobsite inclusions in the bixbyite bulk, it is necessary to discuss the crystallization conditions in more detail, as given in the following. Mineralization that occurred in the Thomas Mountain Range is generally consid-

FIGURE 8. (a) TEM bright-field image of the $1 \times 1 \mu\text{m}$ area mapped with the ACOM system. Several precipitates in contact or close to a braunite lamella are visible, many displaying their characteristic rectangular shape. In **b**, a combination of the phase and reliability mapping is depicted, with darker areas corresponding to lower reliability (most notably at grain boundaries). Most of the crystallites visible in **a** were indexed as jacobsite (green) by the software, whereas several (marked with arrows, compare **a**) were indexed as bixbyite with high reliability. (**c**, **d**, and **e**) The orientations of the mapped precipitations corresponding to the color code depicted in (**f**) and combined with the orientation reliability are shown. The bixbyite/braunite lattice is uniformly oriented along its $[010]$ zone axis and consequently not displayed for easier visibility of the spinels. Scale bars are 200 nm.



ered to be of miarolitic origin (Burt et al. 1982; Christiansen et al. 1983, 1984), whereas Mason described the formation of bixbyite specimens to be of fumarolitic or pneumatolytic origin (Mason 1944). Hot and water-rich magmatic fluids rise to the surface along seams and cracks of the cooling magmatic host rock, inducing mineralization under low-pressure and high-temperature conditions. According to Mason, temperatures of over $800 \text{ }^\circ\text{C}$ are needed for

the formation of iron-rich (>45 at% of cations) bixbyites like those found in the Thomas Mountain Range, which agrees well with the temperatures of the rhyolitic magma proposed by Bikun, ranging between 630 and $850 \text{ }^\circ\text{C}$ (Bikun 1980). The phase diagram of the manganese and iron oxide system, reported by Crum and depicted in Figure 10, shows that for bixbyites with roughly 50 mol% of Fe_2O_3 , three different phase fields might have been reached, depend-

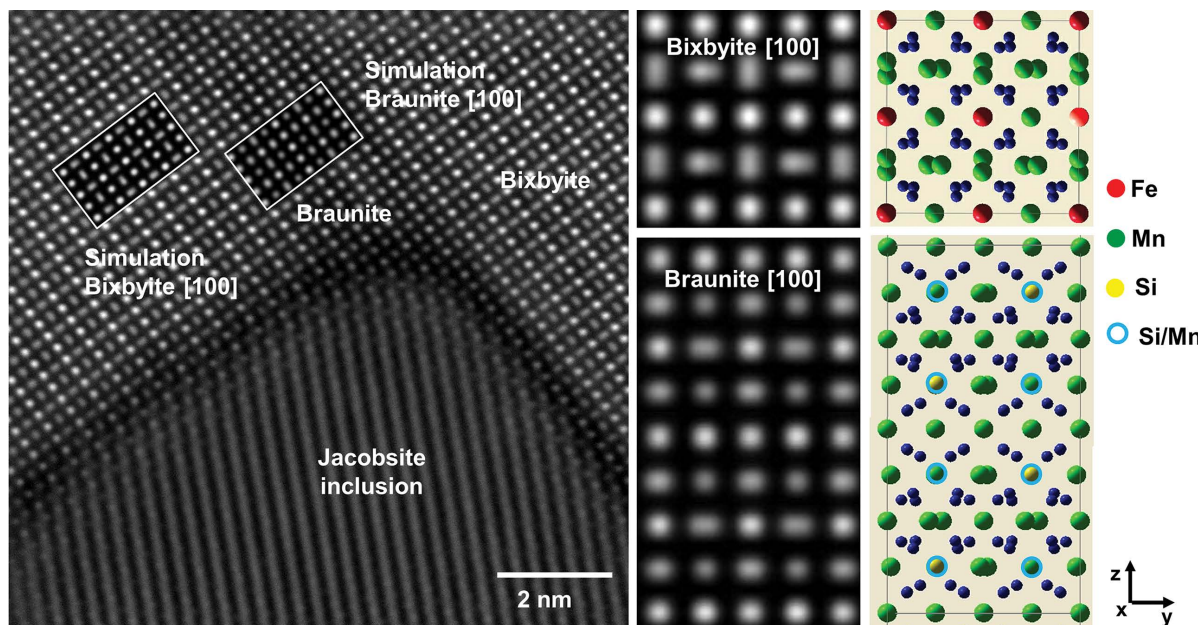


FIGURE 9. Bixbyite host matrix with epitaxial braunite lamella and jacobsite inclusion. Simulations of the bixbyite and braunite structure are shown (also as inset) in addition to the corresponding atom positions in the unit cells [created with QSTEM (Koch 2002) and VESTA software (Momma and Izumi 2008)].

ing on the respective temperature (Crum et al. 2009).

Only for temperatures slightly above 950 °C, crystallization of jacobsite spinel in addition to bixbyite is possible for the given composition, represented by a small two-phase field. Below this temperature, bixbyite plus hematite will form, both of which are commonly occurring minerals at various locations in and around the Thomas Mountain Range. Since the phase diagram describes temperatures in a dry system, the influence of water activity might have reduced the temperature needed for spinel formation, consequently enabling the crystallization of jacobsite even at postulated magma temperatures of 850 °C max. However, in this case, jacobsite would be expected to be a commonly found mineral at this location due to the generally fluid-rich environment. Moreover, it is seen as likely that discrete jacobsite crystals in close proximity to the large bixbyite crystals would have been formed rather than the observed intergrowth with bixbyite host. Nevertheless, a bixbyite-spinel paragenesis has not been reported for the Thomas Mountain Range/Solar Wind Claim. It should also be noted that no jacobsite inclusions were observed in the third sample of this study, prepared from a smaller bixbyite crystal of a locality being some miles away from the Solar Wind Claim, which indicates the spinel formation to be a rather local phenomenon. The uniformly small size of the jacobsite crystallites indicates that conditions supporting spinel nucleation and growth only lasted for a comparably short duration. Considering these observations, the jacobsite formation as a consequence of water activity appears to be unlikely, and it is expected to be a solid-state reaction inside the bixbyite host crystals. In this case, the potential water activity can be ruled out since the bixbyite crystal, being nominally anhydrous (Keppler and Smyth 2006) represents a closed system. Therefore, it is concluded that the jacobsite-bearing bixbyite crystals of the Solar Wind Claim have experienced slightly higher temperature conditions, sufficient

for a solid-state spinel nucleation within the host crystals, possibly triggered by a local second lava outflow with higher temperature. Furthermore, since the influence of water is ruled out, the occur-

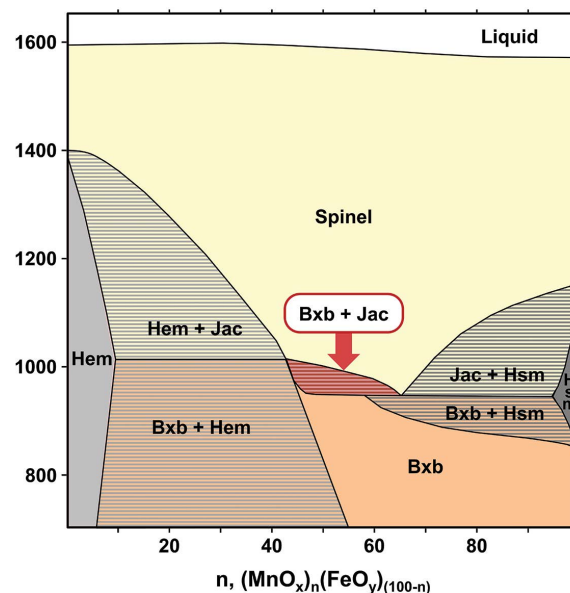


FIGURE 10. $\text{MnO}_x\text{-FeO}_y$ binary phase diagram, redrawn after Crum et al. (2009). Only at a high temperature of ~950 °C, a rather small two-phase field (highlighted in red), where bixbyite and jacobsite coexist, was reported. Hsm stands for tetragonal hausmanite Mn_3O_4 , Hem = hematite Fe_2O_3 , Jac = jacobsite, Bxb = bixbyite, and spinel, which was considered by Crum et al. (2009) as a solid solution of jacobsite, iwakiite MnFe_2O_4 (= jacobsite-Q, tetragonal, space group no. 141: $I4_1/amd$), and magnetite Fe_3O_4 .

rence of jacobsonite serves as kind of a rough geo-thermometer, indicating a locally higher peak temperature of >850 °C, which also accounts for the exceptional size of the bixbyites from the Solar Wind Claim, compared to other locations, since a higher peak temperature and a correspondingly longer cooling period promotes both diffusion and exaggerated grain growth. Finally, the TEM results show that the nucleated nano-crystallites have no specific orientation with respect to the host crystal, and when in contact with braunite lamellae, they were forced into the typically observed rectangular shape, being a clear indication for a unique exomorphism of jacobsonite via the braunite lamellae.

IMPLICATIONS

Only by employing today's state-of-the-art high-resolution TEM/STEM analysis in conjunction with structure simulations and electron diffraction, the observed nanosized precipitates within the bixbyite host crystal could be unequivocally identified as jacobsonite crystallites. This indicates that such investigations on the atomic scale are even relevant for large-scale petrogenetic processes and hence have implications on the determined formation temperature of the host rock. Moreover, as it is the case here, the identification of jacobsonite nanocrystals pointed to a secondary heat-treatment event, which initiated the precipitation via a solid-state reaction.

The combination of atomic scale imaging and chemical analysis with very high lateral resolution allowed for detailed insights into atomic processes that occurred during the crystallization of the host crystals and, in addition, upon their formation. Only the application of such advanced electron microscopy techniques enabled us, for the first time, to verify the presence of jacobsonite in the Thomas Mountain Range and to identify the driving force for exaggerated bixbyite grain growth, i.e., formation at a considerably higher temperature. The observation of bixbyite with jacobsonite precipitations can thus be employed as a helpful mineral assemblage in terms of geo-thermometry with a relatively narrow temperature window.

Finally, the intergrowth of randomly oriented nanometric spinel precipitates inside a bixbyite single crystal resembles a composite of two interesting structure types that might exhibit new or improved electrical or magnetic properties. Moreover, the processes that lead to the formation of the statistically oriented jacobsonite nanocrystals inside a bixbyite single crystal are of interest, offering the possibility of new oxide ceramics with interesting ferroelectric and ferromagnetic properties.

ACKNOWLEDGMENTS

This project was fun but not funded. All work was done by the authors, including the collection and preparation of the sample material.

REFERENCES CITED

Abs-Würmbach, I. (1980) Miscibility and compatibility of braunite, $Mn^{2+}Mn^{3+}_2O_5/SiO_2$, in the system Mn-Si-O at 1 atm in air. *Contributions to Mineralogy and Petrology*, 71, 393–399.

Arminoff, G. (1931) Lattice dimensions and space group of braunite. *Svenska Vetenskapsakademiens Handlingar*, 9, 14–22.

Beard, J.S., and Tracy, R.J. (2002) Spinel and other oxides in Mn-rich rocks from the Hutter Mine, Pittsylvania County, Virginia, U.S.A.: Implications for miscibility and solvus relations among jacobsonite, galaxite, and magnetite. *American Mineralogist*, 87, 690–698.

Bikun, J.V. (1980) Fluorine and lithophile element mineralization at Spor Mountain, Utah. M.Sc. thesis, Arizona State University.

Burt, D.M., Sheridan, M.F., Bikun, J.V., and Christiansen, E.H. (1982) Topaz rhyolites; distribution, origin, and significance for exploration. *Economic Geology*, 77, 1818–1836.

Byström, A., and Mason, B. (1943) The crystal structure of braunite, $3Mn_2O_3 \cdot MnSiO_3$. *Arkiv Kemi, Minerali och Geologi*, 16, 1–8.

Christiansen, E.H., Burt, D.M., Sheridan, M.F., and Wilson, R.T. (1983) The petrogenesis of topaz rhyolites from the western United States. *Contributions to Mineralogy and Petrology*, 83, 16–30.

Christiansen, E.H., Bikun, J.V., Sheridan, M.F., and Burt, D.M. (1984) Geochemical evolution of topaz rhyolites from the Thomas Mountains range and Spor Mountain. *American Mineralogist*, 69, 223–236.

Crum, J.V., Riley, B.J., and Vienna, J.D. (2009) Binary phase diagram of the manganese oxide-iron oxide system. *Journal of the American Ceramic Society*, 92, 2378–2384.

Dachs, H. (1956) Die Kristallstruktur des Bixbyits $(Fe, Mn)_2O_3$. *Zeitschrift für Kristallographie—Crystalline Materials*, 107.

de Villiers, J.P.R. (1980) The crystal structure of braunite-II and its relation to bixbyite and braunite. *American Mineralogist*, 65, 756–765.

de Villiers, J.P., and Buseck, P.R. (1989) Stacking variations and nonstoichiometry in the bixbyite-braunite polysomatic mineral group. *American Mineralogist*, 74, 1325–1336.

de Villiers, P.R., and Herbstein, F.H. (1967) Distinction between two members of the braunite group. *American Mineralogist*, 52, 20–30.

Essene, E.J., and Peacor, D.R. (1983) Crystal chemistry and petrology of coexisting galaxite and jacobsonite and other spinel solutions and solvi. *American Mineralogist*, 68, 449–455.

Fleischer, M. (1943) A discussion bixbyite-sitaparite-partridgeite. *American Mineralogist*, 28, 468–469.

Goldschmidt, V.M. (1926) *Geochemische Verteilungsgesetze der Elemente IV: Zur Kristallstruktur der Oxyde der seltenen Erdmetalle*. Norsk videnskaps-akademi i Oslo. Skriftr. I. Matematisk-naturvidenskabelig klasse, 5, 1–24.

Gottesmann, W., Gottesmann, B., Seifert, W., and Unger, H. (2015) The jacobsonite-magnetite series at the Tumurtijn-ovoo Fe-Mn-Zn skarn deposit, Mongolia. *Neues Jahrbuch für Mineralogie—Abhandlungen: Journal of Mineralogy and Geochemistry*, 192, 289–306.

Grazulis, S., Chateigner, D., Downs, R.T., Yokochi, A.F.T., Quiros, M., Lutterotti, L., Manakova, E., Butkus, J., Moeck, P., and Le Bail, A. (2009) Crystallography open database—an open-access collection of crystal structures. *Journal of Applied Crystallography*, 42, 726–729.

Haidinger, W. (1828) Mineralogical account of the ores of manganese. *Transactions of the Royal Society of Edinburgh*, 11, 119–142.

Keppeler, H., and Smyth, J.R., Eds. (2006) *Water in Nominally Anhydrous Minerals*, vol. 62, 478 p. *Reviews in Mineralogy and Geochemistry*, Mineralogical Society of America, Chantilly, Virginia.

Kleber, W. (1957) Zur Adsorptionstheorie der Exomorphose. *Zeitschrift für Kristallographie—Crystalline Materials*, 109.

Kleebe, H.-J., and Lauterbach, S. (2008) Exaggerated grain growth in bixbyite via fast diffusion along planar defects. *Crystal Research and Technology*, 43, 1143–1149.

Koch, C.T. (2002) Determination of core structure periodicity and point defect density along dislocations. Ph.D. thesis, Arizona State University. ProQuest Dissertations and Theses.

Lucchesi, S., Russo, U., and Della Giusta, A. (1996) Crystal chemistry and cation distribution in some Mn-rich natural and synthetic spinels. *European Journal of Mineralogy*, 9, 31–42.

Mason, B. (1944) The system $Fe_2O_3-Mn_2O_3$: Some comments on the names bixbyite, sitaparite and partridgeite. *American Mineralogist*, 29, 66–69.

Menzer, G. (1949) Über die Mehrdeutigkeit der Kristallstrukturbestimmung. *Zeitschrift für Naturforschung A*, 4, 11–21.

Momma, K., and Izumi, F. (2008) VESTA: A three-dimensional visualization system for electronic and structural analysis. *Journal of Applied Crystallography*, 41, 653–658.

Moore, P., and Araki, T. (1976) Braunite, its structure and relationship to bixbyite and some insights on the genealogy of fluorite derivative structures. *American Mineralogist*, 61, 1226–1240.

Patterson, A.L. (1939) Homometric structures. *Nature*, 143, 939–940.

Pauling, L., and Shappell, M.D. (1930) The crystal structure of bixbyite and the C-modification of the sesquioxides. *Zeitschrift für Kristallographie—Crystalline Materials*, 75, 128–142.

Penfield, S.L., and Foote, H.W. (1897) On bixbyite, a new mineral, and notes on the associated topaz. *American Journal of Science*, 4, 105–110.

Rauch, E.F., and Véron, M. (2014) Automated crystal orientation and phase mapping in TEM. *Materials Characterization*, 98, 1–9.

Strunz, H., and Nickel, E.H. (2001) *Strunz Mineralogical Tables: Chemical-structural Mineral Classification System*, 9th ed., 870 p. Schweizerbart, Stuttgart.

Zachariasen, W. (1928) Über die Kristallstruktur von Bixbyit sowie künstlichem Mn_2O_3 . *Crystalline Materials*, 67, 455–464.

MANUSCRIPT RECEIVED JULY 13, 2020

MANUSCRIPT ACCEPTED FEBRUARY 10, 2021

MANUSCRIPT HANDLED BY AARON LUSSIER